International Journal of Heat and Mass Transfer 51 (2008) 5906–5917

Contents lists available at ScienceDirect

International Journal of Heat and Mass Transfer

journal homepage: www.elsevier.com/locate/ijhmt

Numerical simulations of interrupted and conventional microchannel heat sinks

Jinliang Xu [a,*], Yanxi Song [a,b], Wei Zhang [a], Hua Zhang [c], Yunhua Gan [d]

[a] Micro Energy System Laboratory, Key Laboratory of Renewable Energy and Gas Hydrate, Guangzhou Institute of Energy Conversion, Chinese Academy of Science, Guangzhou 510640, PR China
[b] Graduate School of Chinese Academy of Science, Beijing 100080, China
[c] Institute of Refrigeration and Cryogenics, University of Shanghai for Science and Technology, Shanghai, PR China
[d] School of Electric Power, South China University of Technology, Wushan Road, Guangzhou 510641, PR China

ARTICLE INFO

Article history:
Received 26 December 2007
Received in revised form 23 April 2008
Available online 1 July 2008

Keywords:
Numerical simulation
Microchannel heat sink
Heat transfer enhancement
Pressure drop reduction

ABSTRACT

We provide three-dimensional numerical simulations of conjugate heat transfer in conventional and the newly proposed interrupted microchannel heat sinks. The new microchannel heat sink consists of a set of separated zones adjoining shortened parallel microchannels and transverse microchambers. Multi-channel effect, physical property variations, and axial thermal conduction are considered. It is found that flow rate variations in different channels can be neglected, while heat received by different channels accounts for 2% deviations from the averaged value when the heat flux at the back surface of the silicon chip reaches 100 W/cm^2. The computed hydraulic and thermal boundary layers are redeveloping in each separated zone due to shortened flow length for the interrupted microchannel heat sink. The periodic thermal developing flow is responsible for the significant heat transfer enhancement. Two effects influence pressure drops across the newly proposed microchannel heat sink. The first one is the pressure recovery effect in the microchamber, while the second one is the head loss when liquid leaves the microchamber and enters the next zone. The first effect compensates or suppresses the second one, leading to similar or decreased pressure drop than that for the conventional microchannel heat sink, with the fluid Prandtl number larger than unity.

1. Introduction

There are two types of boundary layer developments in channels: the hydraulic and thermal boundary layers [1]. Assuming that the classical theory of fluid flow and heat transfer is still valid in microchannels, the hydrodynamic and thermal entrance lengths are $L_{h,e} = 0.055ReD_h$ and $L_{T,e} = 0.055RePrD_h$, respectively. Considering water flowing in a 100 μm microtube with *Re* of 1000 and *Pr* of 3.54 at the temperature of 50 °C, the two lengths are 5.5 mm and 19.47 mm, which may be on the same order of the chip length that is expected to be cooled by microchannel passages, inferring that the entrance effects should be considered.

Mishan et al. [2] studied the developing flow in rectangular microchannels of $D_h = 440$ μm, with water as the working fluid. An Infrared Radiation Image system was used to determine the bulk fluid temperatures along microchannels. Their experimental results of pressure drop and heat transfer confirm that including the entrance effects, the classical theory is applicable for water flow in microchannels. They demonstrated that the data provided by some investigators can be caused by the entrance effect and highlighted the importance of common phenomena that are often neglected for standard flows such as inlet velocity profile, axial thermal conduction, effect of inlet and outlet manifolds.

Al-Bakhit and Fakheri [3] noted that in microchannel heat exchangers, short lengths and comparatively thick walls through which heat is conducted preclude the existence of fully thermal developed flow over a large portion of the heat exchanger. They concluded that there is a significant change in the overall heat transfer coefficient in the developing region and the three-dimensional heat transfer in the microchannel heat exchanger should be considered.

Gamrat et al. [4] performed both two and three-dimensional numerical analysis of convective heat transfer in microchannels. Giving the thermal entrance effect considered, the numerical analysis did not find any significant scale effect on the heat transfer in microchannels with the hydraulic diameter down to 100 μm.

Morini and Spiga [5] studied the viscous dissipation for liquids flowing in heated microchannels by the conventional theory. A correlation between the Brinkman number and the Nusselt number for silicon ⟨100⟩ and ⟨110⟩ microchannels was given. It is demonstrated that the fluid is of importance in establishing the exact limit of significance of viscous dissipation in microchannels. Morini and Baldas [6] demonstrated that the viscous dissipation cannot

* Corresponding author.
E-mail address: xujl@ms.giec.ac.cn (J. Xu).

0017-9310/$ - see front matter © 2008 Elsevier Ltd. All rights reserved.
doi:10.1016/j.ijheatmasstransfer.2008.05.003

Nomenclature

A_{film}	effective thin film heater area (m^2)
A_w	two side wall surface area of a single triangular microchannel with the heating length of L_h (m^2)
C_p	specific heat (J/kg K)
D_h	hydraulic diameter (m)
f	Darcy friction factor
G	mass flux (kg/m^2 s)
h	heat transfer coefficient (W/m^2 K)
I, J	maximum grid numbers in x and y directions for the temperatures in the heating area
L	length of the microchannel (m)
L_h	effective heating length of the thin film heater (m)
$L_{h,e}$	hydrodynamic entrance length (m)
$L_{T,e}$	thermal entrance length (m)
M	flow rate (kg/s)
N	number of parallel microchannels
Nu	local Nusselt number at the internal side wall surface of the triangular channel
Nu_H	Nusselt number for the fully developed flow at the constant heat flux condition
Nu_m	average Nusselt number over the entire silicon chip
Nu_x	cross-sectional averaged, but flow direction dependent Nusselt number
n	attached coordinate perpendicular to the wall surface of the triangular channel (m)
p	pressure (Pa)
p_r	reduced pressure equal to the pressure subtracting the atmosphere pressure (Pa)
Pe	Peclet number
Po	Poiseuille number
Pr	Prandtl number of water
Q	net heat received by fluid (W)
q	project heat flux on the effective heating film (W/m^2)
q_{sw}	Heat flux on the two side walls of the triangular microchannels (W/m^2)
Re	Reynolds number
s	integration length index along the internal wall surface of the cross section (m)
T	temperature (K or °C)
T_{fmax}	the maximum water temperature in a specific cross section (°C)
$T_{f,bulk}$	cross-sectional liquid temperature (°C)
T_{iw}	temperature at the local internal side wall surface of the triangular channel (°C)
T_w	temperature at the local thin film heating area (°C)
v_x, v_y, v_z	velocity in x, y and z coordinate (m/s)
$v_{x,a}$	average velocity in the inlet plenum (m/s)
$v_{x,m}$	average axial velocity in the triangular microchannel (m/s)
$v_{x,max}$	maximum axial velocity perpendicular to the side wall surface (m/s)
W	width of the inlet fluid plenum (m)
W_s	width of the side wall of the triangular microchannel (m)
W_t	top width of the triangular channel (m)
x, y, z	three coordinates shown in Fig. 1 (m)
x^+	the non-dimensional flow length for the thermal boundary layer development
ρ	density (kg/m^3)
μ	dynamic viscosity ($Pa \cdot s$)
ν	kinematic viscosity (m^2/s)
λ	thermal conductivity (W/mK)
θ	base angle of the triangular channels relative to the base plane
ΔT_m	average temperature difference between that at the thin film heating area and the average liquid temperature in channels (°C)
ΔT_{film}	heating film temperature difference between the conventional and interrupted microchannel heat sinks (K)
Δp	pressure drop (Pa)
δ	thickness of the etched channel depth (m)
δ_c	thermal boundary layer thickness (m)
δ_f	hydraulic boundary layer thickness (m)
δ_{max}	the thickness at which $v_{x,max}$ is reached (see Fig. 3) (m)
ϕ	viscous dissipation term
τ_w	cross-sectional integrated shear stress at the solid wall surface (Pa)

Subscripts

CFD	computational fluid dynamics simulation
EXP	experimental measurement value
f	fluid
m	average mean value
o'	original point attached on the center side wall surface of the triangular channel
s	solid silicon
in	inlet
out	outlet
w	wall surface condition

be neglected for the microchannel hydraulic diameter less than 50 μm for the liquid flows. Other studies on the viscous dissipation can be found by Morini [7], Koo and Kleinstreuer [8], etc.

Liu et al. [9] studied fluid flow and heat transfer in microchannel cooling passages. The velocity field was found to be coupled with the temperature distribution and distorted through the variations of the viscosity and the thermal conductivity. The heat transfer enhancement due to the viscosity variation is significant, even though the axial conduction caused by the thermal conductivity variation was insignificant unless for the very low Reynolds number. Li et al. [10] studied the fluid flow and heat transfer in microchannels. The bulk liquid temperatures vary in a quasi-linear form along the flow direction for the high liquid flow rates, but not for the low flow rates.

The pumping requirement is another issue is to be evaluated for microchannel heat sinks, which is noted to be very high by Garimella and Singhal [11]. None of the micropumps is really suitable for this application in the literatures. In their work, the microchannel size is optimized for the minimum pumping requirement.

In our previous study [12], we proposed a new silicon microchannel heat sink, composing of parallel longitudinal microchannels and several transverse microchambers, separating the whole flow length into several independent zones, in which the thermal boundary layer is developing. The repeated thermal developing flow ensures the heat transfer enhancement. Experimental results are given for both benefits of the heat transfer enhancement and the pressure drop reduction, compared with the conventional microchannel heat sink.

The present paper focuses on numerical computations of interrupted and conventional microchannel heat sinks. Because there are many factors influencing the flow and heat transfer in microchannels, complete three-dimensional computations were performed, considering all the details of the two microchannel heat sinks. The objective of the paper is to identify the mechanisms of

heat transfer enhancement and pressure drop reduction for the newly proposed microchannel heat sink. Especially, the developments of hydraulic and thermal boundary layers along microchannels are focused.

2. Description of the interrupted and conventional microchannel heat sinks

Fig. 1a shows the conventional microchannel heat sink and Fig. 1b shows the newly proposed one. They are similar in geometries, except that the later one has five transverse trapezoid microchambers, separating the entire longitudinal microchannels into six separated zones (see Fig. 1b). The two silicon wafers have the overall length of 30.0 mm and width of 7.0 mm, with the thickness of 525 μm, bonded with a 7740 glass cover plate. The 10 longitudinal microchannels are 21.45 mm in length, covering the total width of 4.35 mm. A single microchannel has the width of 300 μm and the depth of 212 μm, forming the hydraulic diameter of 155.4 μm. The pitch distance of the two longitudinal microchannel is 150 μm. Fig. 1c shows the channel number and the cross section of A–A corresponding to Fig. 1a. As shown in Fig. 1d, the transverse microchamber has the trapezoid cross section with the top width of 1015 μm, the bottom width of 715 μm, with the same etched depth as those of the longitudinal microchannels.

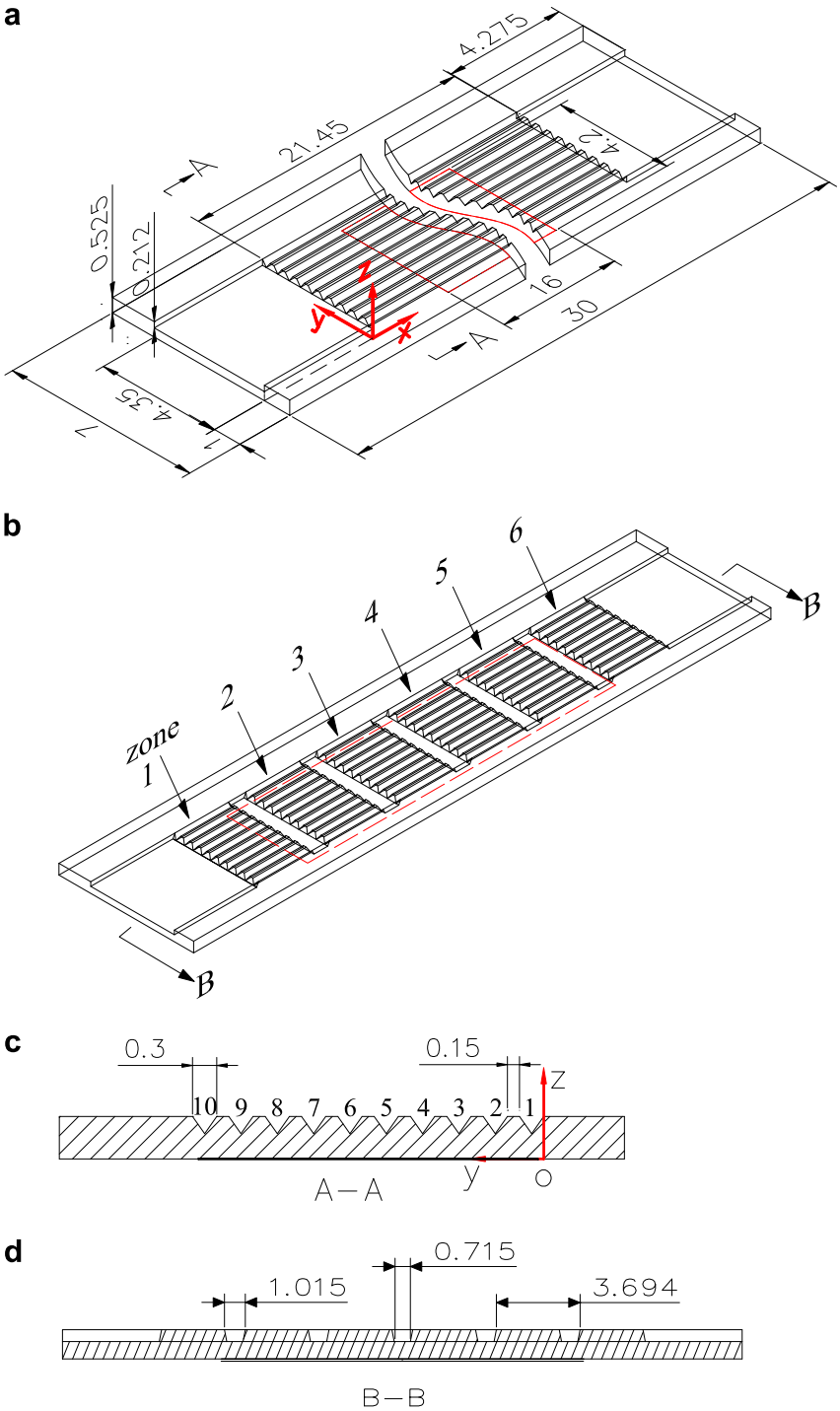

Fig. 1. Two microchannel heat sinks (all dimensions are in millimeter).

At the back surface of the silicon substrate, a thin platinum film was deposited to provide a uniform heat flux. The effective heating area is 16.0 mm in length, covering the zones of 2, 3, 4 and 5. The heating width is 4.20 mm, which is slightly narrower than the total width of the ten longitudinal microchannels.

The three-dimensional coordinate system was shown in Fig. 1a, which is the same for the interrupted microchannel heat sink shown in Fig. 1b. The axial flow direction, the width and the chip thickness are referred as x, y and z coordinates, respectively. The original point of (0,0,0) is at the back surface of the silicon chip, and is in the corner of the junction surface of the inlet fluid plenum and the longitudinal microchannel. Because computations were performed over the entire silicon chip, the computation domain covers both the negative and positive axial coordinate values.

3. Description of the experiment

The experiments were performed at Guangzhou Institute of Energy Conversion, Chinese Academy of Science. The detailed experiment setup and procedure were described in Xu et al. [12]. Water is used as the working fluid, and flows through a liquid valve, a 2 μm filter, the silicon wafer, a heat exchanger, and is finally collected in a glass beaker. The upstream liquid was driven by a nitrogen gas tank with precisely controlled pressures. The measurement parameters involve the upstream pressure of the silicon chip, pressure drop across the silicon chip, flow rate, upstream and downstream fluid temperatures of the silicon chip, and wafer temperatures. We used an Infrared Radiation Image system to measure the back surface temperatures of the silicon chip. Throughout all the tests, the IR camera was situated so that the heating area of the silicon wafer (16.0 mm by 4.2 mm) is in the field of view. Using this technique, the temperature gradient and maximum temperature could be precisely obtained continuously. Table 1 shows the parameter uncertainties for the experiment cited from Xu et al. [12].

Table 1
The maximum errors

Parameters	Maximum errors (%)	Parameters	Maximum errors (%)
D_h	1.29	Δp	0.1%
L	0.01	T	0.5 °C (1.67)
M	1.02	Nu	2.93
f	3.33	Re	2.96

4. Three-dimensional numerical simulations over the entire silicon chip

In order to fully understand the liquid flow and heat transfer in the two microchannel heat sinks, the three-dimensional conjugate heat transfer between silicon and liquid was computed over the entire silicon chip. The numerical simulations consider: (1) the developing flow and heat transfer in microchannels, (2) steady, laminar flow and heat transfer, (3) varied fluid thermalphysical properties except the density, (4) axial thermal conductivity, (5) viscous dissipation, (6) multi-channel effect (all the channels are involved in the computations).

The mass, momentum and energy equations are written for water as

$$\nabla \cdot \mathbf{v} = 0 \tag{1}$$

$$\rho_f \frac{\partial (v_i v_j)}{\partial x_j} = -\frac{\partial p}{\partial x_i} + \frac{\partial}{\partial x_j}\left[\mu_f \left(\frac{\partial v_i}{\partial x_j} + \frac{\partial v_j}{\partial x_i}\right)\right], \quad i = 1,2,3 \tag{2}$$

$$\rho_f \mathbf{v} \cdot \nabla (C_{pf} T) = \nabla \cdot (\lambda_f \nabla T) + \phi \tag{3}$$

In Eq. (2), x_1, x_2 and x_3 are referred as x, y and z coordinate respectively, ϕ is the viscous dissipation term, which is written as

$$\phi = \mu_f \left[2\left(\frac{\partial v_x}{\partial x}\right)^2 + 2\left(\frac{\partial v_y}{\partial y}\right)^2 + 2\left(\frac{\partial v_z}{\partial z}\right)^2 + \left(\frac{\partial v_y}{\partial x} + \frac{\partial v_x}{\partial y}\right)^2 + \left(\frac{\partial v_z}{\partial y} + \frac{\partial v_y}{\partial z}\right)^2 + \left(\frac{\partial v_x}{\partial z} + \frac{\partial v_z}{\partial x}\right)^2 \right] \tag{4}$$

The energy conservation equation for silicon is written as

$$\nabla \cdot (\lambda_s \nabla T) = 0 \tag{5}$$

The above four equations are fully coupled due to the varied physical properties of liquid and silicon. The physical properties of water (C_{pf}, λ_f, μ_f) and thermal conductivity of silicon λ_s depend on temperatures, and are cited from Incropera [13]. Silicon has the thermal capacity of 730 J/kg, which is set as a constant in the computations.

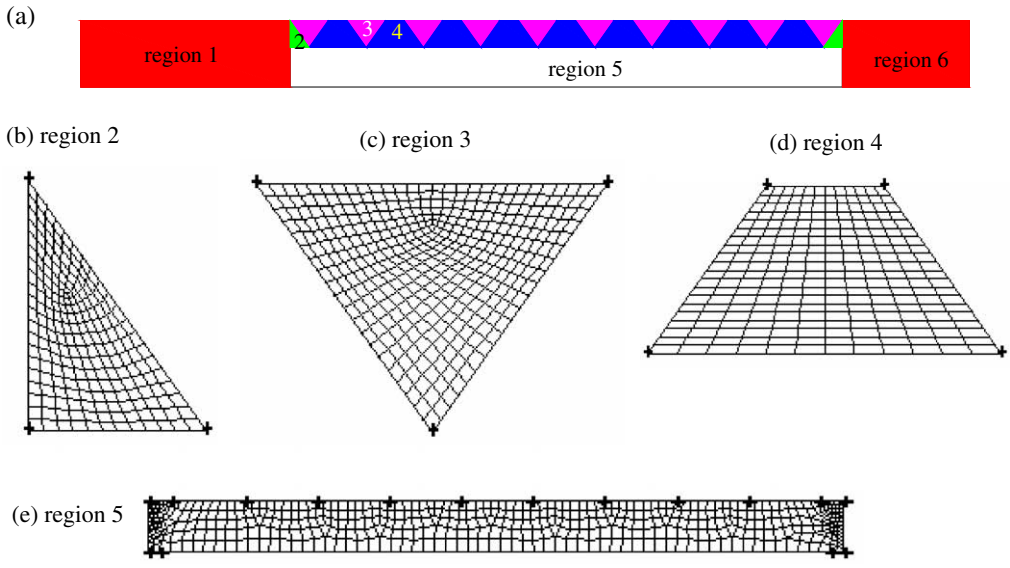

Fig. 2. Grid generations in a cross section of the silicon chip.

4.1. Boundary conditions

(1) The flow is uniform at the entrance of the inlet fluid plenum, i.e., $v_x = v_{x,a}$. The liquid temperature there is given by the measured value. The flow is assumed to reach the atmosphere pressure at the silicon chip exit.
(2) Uniform heat flux is applied at the heating area of 16.0×4.2 mm. The top surface of the silicon substrate bonded with the Pyrex glass is adiabatic. Other surfaces exposed in the air environment except the heating film, have the assumed natural convection heat transfer coefficient of 10 W/m^2 K with the surrounding air. Such procedure is similar to that used by Gamrat et al. [4]. Numerical simulations show that the natural heat transfer coefficient has small effect on the flow and heat transfer in microchannels.

4.2. Grid generations

Fig. 2a shows a cross section of the conventional microchannel heat sink. The computational domain is divided into six regions, with regions 1, 2, 4, 5 and 6 for the silicon, region 3 for the liquid. Because there are ten longitudinal microchannels, regions 3 and 4 are repeated consecutively. Rectangular structured grids are used for regions 1 and 6. Grids on the margin of the regions depend on the neighboring regions. Fig. 2(b–e) shows the unstructured grids for regions 2, 3, 4 and 5 respectively.

The interrupted microchannel heat sink has similar grids as that of the conventional one. However, grids at the entrance of each separated zone are denser (see Fig. 1b). The interrupted microchannel heat sink has 300 grids in x coordinate, 300 girds for liquid and 90 grids for solid in y coordinate, 20 grids for liquid and 16 grids for solid in z coordinate. The total grid number is 1.8 million. The total grid number is 1.6 million for the conventional microchannel heat sink.

The sensitivity analysis of grids was performed. For the conventional microchannel heat sink, 0.6, 0.9 and 1.2 million grids are tried, at which the average Nusselt numbers deviate 5.5%, 3.2% and 1.2% from that of 1.6 million grids. For the interrupted microchannel heat sink, deviations of the average Nusselt numbers using 0.6, 0.9, 1.2 and 1.6 million grids from that using 1.8 million grids are 7.2%, 4.3%, 2.2% and 0.9% respectively. Thus we use 1.6 million grids for the conventional microchannel heat sink, and 1.8 million grids for the interrupted one. It is noted that the margin width of region 1 is slightly larger than that of region 6, thus we did not use the symmetry boundary condition to reduce the computation domain but computed the whole silicon chip.

4.3. Running the software

The commercial software of FLUENT 6.0 is used. The SIMPLE method is used for the computations. The second order upwind scheme is used for the momentum and energy conservation equations. Smaller Reynolds number leads to larger variations of physical properties of silicon and liquid at the given heat flux. Thus a smaller relaxation factor is needed to reach the convergence of the computations. In this study, the relaxation factor is in the range of 0.2–0.8 for the momentum and energy equations. The convergence criterion is

$$\sum\sum |\mathbf{v}_i(x,y,z) - \mathbf{v}_{i,0}(x,y,z)| \leqslant 10^{-6} \quad (6)$$

$$\sum\sum |T(x,y,z) - T_0(x,y,z)| \leqslant 10^{-9} \quad (7)$$

Note that the subscript i can be x, y or z.

5. Parameter definitions

Parameter definitions are needed to characterize the flow and heat transfer in microchannel heat sinks. Even though the two microchannel heat sinks have different structures, the parameter definitions are similar.

The measured parameters are the total flow rate of M, the effective heating power of Q, the inlet and outlet liquid temperature of T_{in} and T_{out}, and the pressure drop across the silicon chip of Δp. The Q is computed as $Q = M/(C_{pf,out}T_{out} - C_{pf,in}T_{in})$. The above parameters involve the following new parameter definitions:

Definitions of velocity and mass flux. The uniform axial flow velocity, which is given as the boundary condition at the entrance of the silicon chip, is computed as $v_{x,a} = M/(\rho_f W\delta)$. The average mass flux in the ten triangular microchannels is $G = M/(N \cdot 0.5W_t \cdot \delta)$. Correspondingly, the average mean axial flow velocity in each triangular microchannel is $v_{x,m} = G/\rho_f$. The Reynolds number is computed as $Re = v_{x,m}D_h/v_f$. The Peclet number is $Pe = Re \cdot Pr$. The axial local Reynolds number and Peclet number are computed using the axial bulk liquid temperature to define the liquid physical properties such as v_f and Pr. However, the averaged values of Re_m and Pe_m are computed using the average liquid temperature of $0.5(T_{in} + T_{out})$ to define v_f and Pr.

Poiseuille number and friction factor. If liquid is flowing in the conventional microchannel heat sink, the total pressure drop consists of friction pressure drop in the inlet fluid plenum, entrance head loss, friction pressure drop in microchannels, head loss when the liquid leaves the microchannel, and frictional pressure drop in the outlet fluid plenum. In order to evaluate the accuracy of the present computation, the Poiseuille number is defined as $Po = \tau_w Re/(\rho_f v_{x,m}^2/2)$, where τ_w is written as $\tau_w = \int_{\text{cross section}} \mu_f \frac{dv_x}{dn}\big|_{\text{wall}} ds/(2W_s + W_t)$. The Poiseuille number is only computed for the conventional microchannel heat sink, and it reaches a constant once the hydraulic fully developed flow is reached.The total pressure drop includes the frictional pressure drop plus the extra head loss in microchannels. An equivalent Darcy friction factor is computed as $f = \Delta p \cdot D_h/(L \cdot \rho_f v_{x,m}^2/2)$, which is used for comparisons between the two microchannel heat sinks.

Surface heat flux. Two surface heat fluxes are used in this study. The first is the project heat flux, written as $q = Q/A_{film}$. The second is the average heat flux in terms of the two side walls of triangular microchannels with the heating length of the thin film heater, $q_{sw} = Q/(N \cdot 2 \cdot W_s \cdot L_h)$.

Two boundary layer thicknesses. We computed the thicknesses of the two boundary layers from the flow field and liquid temperature distributions in microchannels. Because there is no big dif-

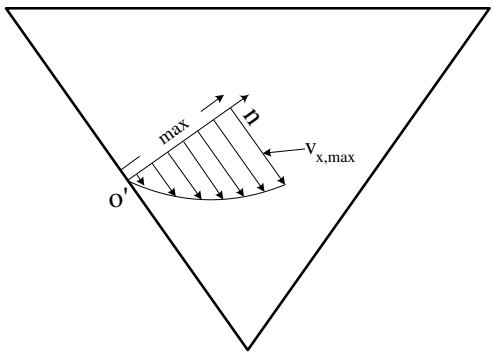

Fig. 3. Computation of the hydraulic boundary layer and thermal boundary layer thickness.

ference for the developments of the two boundary layers among multi-channels, we only compute them for the channel 5 (see Fig. 1c). The thicknesses of the two boundary layers are not uniform in the cross section of microchannels, especially for the thermal boundary layer. The local boundary layers at the center of a channel side wall are focused, where an attached coordinate is fixed (see Fig. 3). The thickness of the hydraulic boundary layer (also named as the displacement thickness) at the center of the side wall is computed as $\delta_f = \int_0^{\delta_{max}} (1 - v_x/v_{x,max})\,dn$. The thickness of the thermal boundary layer (also named as the conduction thickness) is computed as $\delta_c = \lambda_{f,o'}/h_{o'}$, where $h_{o'}$ is given by $h_{o'} = -\lambda_{f,o'} \frac{\partial T}{\partial n}\big|_{o'}/(T_{o'} - T_{f,bulk})$.

Nusselt number. We have three Nusselt numbers. The first is the local Nusselt number at the side wall surfaces of microchannels,

Table 2
Run cases that were computed in the present paper

Run	T_{in} (°C)	T_{out} (°C)	G (kg/m^2 s)	Re_m	Pe_m	Δp_{EXP} (KPa)	Δp_{CFD} (KPa)	Q(W)	q (W/cm^2)	q_{sw} (W/cm^2)
1	30.6	48.9	721.47	169	726	10.278	11.413	17.376	25.8568	20.9085
*1**	*29.8*	*48.4*	*706.26*	*165*	*721*	*10.579*	*11.035*	*17.433*	*25.9413*	*20.9768*
3	30.7	38.2	1830.9	391	1888	30.229	33.965	18.370	27.3363	22.1048
*3**	*30.6*	*38.1*	*1752.26*	*374*	*1807*	*30.093*	*32.049*	*17.556*	*26.1250*	*21.1253*
5	31.0	36.0	2786.10	583	2879	50.067	56.988	18.498	27.5270	22.2591
*5**	*30.7*	*35.8*	*2631.31*	*548*	*2720*	*50.066*	*53.301*	*17.878*	*26.6040*	*21.5127*
17	30.0	62.4	784.95	210	790	10.273	11.071	33.800	50.2973	40.6717
*17**	*27.6*	*58.5*	*831.23*	*210*	*842*	*10.876*	*11.943*	*34.147*	*50.8134*	*41.0890*
19	31.0	45.1	1960.80	450	2006	30.168	33.803	36.833	54.8111	44.3216
*19**	*28.6*	*42.5*	*1856.49*	*405*	*1910*	*30.066*	*31.271*	*34.459*	*51.2785*	*41.4651*
21	31.0	40.5	2953.00	647	3036	50.069	57.106	37.925	56.4365	45.6360
*21**	*31.0*	*41.5*	*2774.85*	*614*	*2850*	*50.026*	*50.141*	*38.813*	*57.7577*	*46.7044*
33	31.7	47.1	3184.9	750	3250	50.072	57.554	65.384	97.2980	78.6777
*33**	*31.3*	*47.7*	*2974.16*	*702*	*3034*	*50.120*	*55.54*	*65.006*	*96.7351*	*78.2225*
70	46.4	60.0	871.13	262	866	10.123	11.386	15.784	23.4876	18.9927
*70**	*46.4*	*57.2*	*1028.79*	*302*	*1026*	*11.502*	*12.663*	*14.643*	*21.7897*	*17.6197*
72	48.9	54.3	2278.20	667	2272	30.591	34.878	16.520	24.5832	19.8786
*72**	*49.0*	*53.7*	*2258.48*	*659*	*2253*	*30.185*	*32.104*	*14.201*	*21.1320*	*17.0879*
74	49.7	53.4	3394.70	994	3386	50.136	57.915	16.368	24.3572	19.6958
*74**	*50.4*	*53.4*	*3369.52*	*992*	*3359*	*50.090*	*53.021*	*13.433*	*19.9899*	*16.1643*

Note: The italics text and the runs with the superscript * represent the parameters for the interrupted microchannel heat sink.

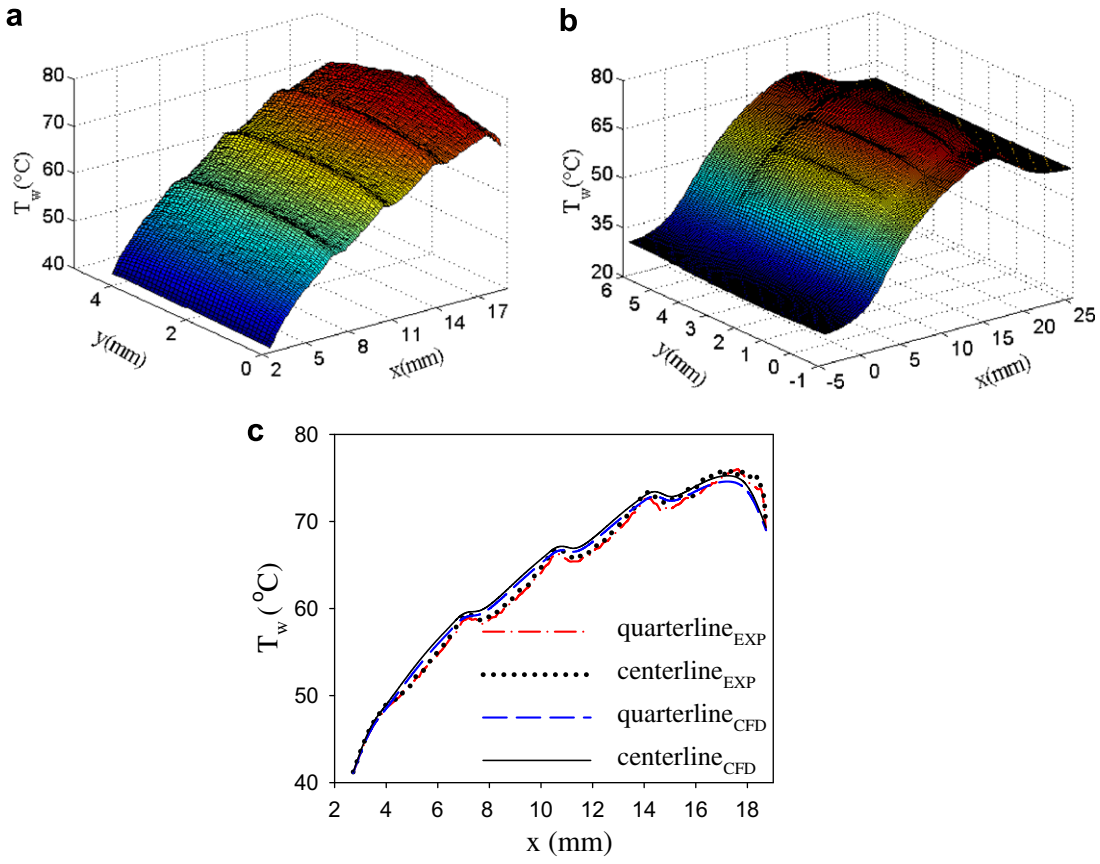

Fig. 4. Measured and computed chip temperature distributions for run 17*. (a) Measurement; (b) computation and (c) measurement and computation at specific width direction; run 17* (Re_m = 210).

$Nu = h \cdot D_h/\lambda_{f,w}$, where h is computed as $h = -\lambda_{f,w}\frac{\partial T}{\partial n}\big|_w/(T_{iw} - T_{f,bulk})$. The second is the axial bulk Nusselt number, written as $Nu_x = \int_{\text{two side walls}} Nu \cdot ds/2W_s$. The top glass cover is adiabatic thus it is not involved in the integration. The average Nusselt number over the whole microchannel heat sink, is computed as $Nu_m = \frac{MD_h(C_{pf,out}T_{out} - C_{pf,in}T_{in})}{N\lambda_{f,m}A_w\Delta T_m}$, ΔT_m is the temperature difference between the thin heating film and the liquid, which is given as $\Delta T_m = T_{w,m} - \frac{1}{2}(T_{in} + T_{out}) = \frac{\sum_{i=1}^{I}\sum_{j=1}^{J}T_{ij}}{IJ} - \frac{1}{2}(T_{in} + T_{out})$, where T_{ij} is the local temperature on the thin heating film at the location of (x_i, y_j), I and J are the maximum grid numbers in x and y directions for the temperatures in the heating area.

Non-dimensional flow length. The non-dimensional flow length for the development of thermal boundary layer is $x^+ = x/(D_h RePr)$.

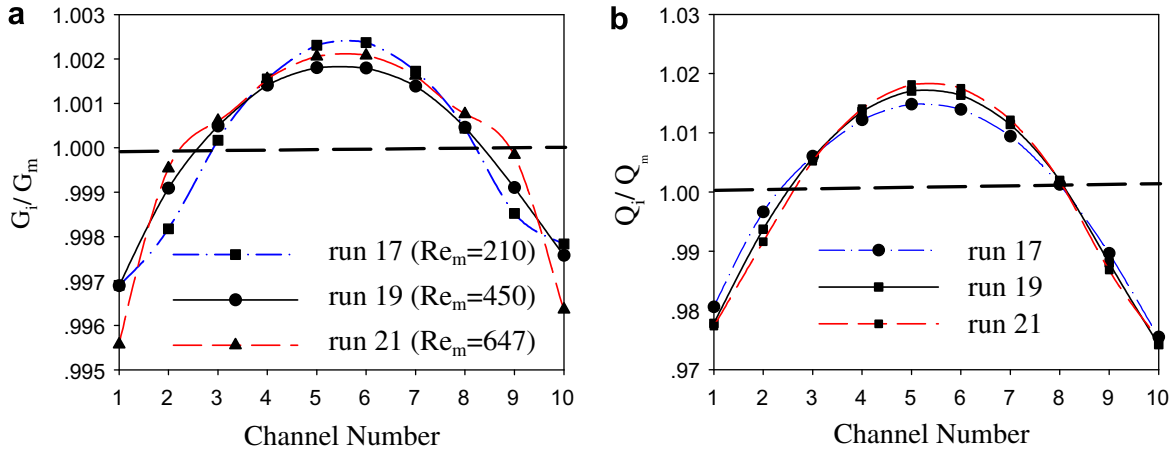

Fig. 5. Multi-channel effect of mass flux and heat for the conventional microchannel heat sink.

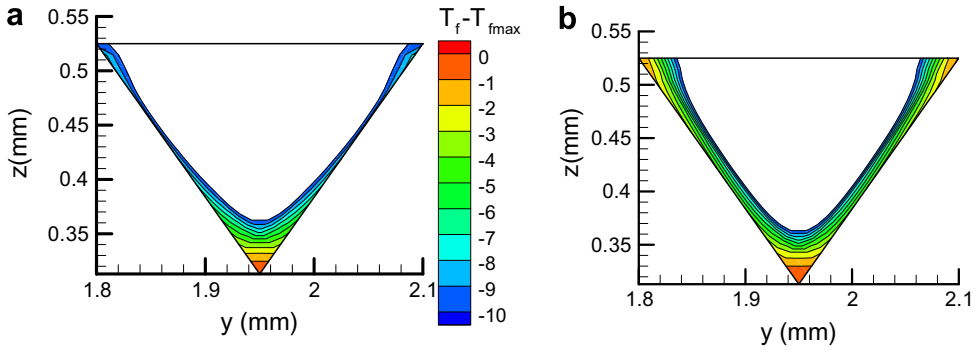

Fig. 6. The temperature field near the solid wall surfaces. (a) Distribution at the entrance of zone 3 for the interrupted microchannel heat sink for run 17* (Re_m = 210); (b) for the conventional microchannel heat sink for run 17 (Re_m = 210).

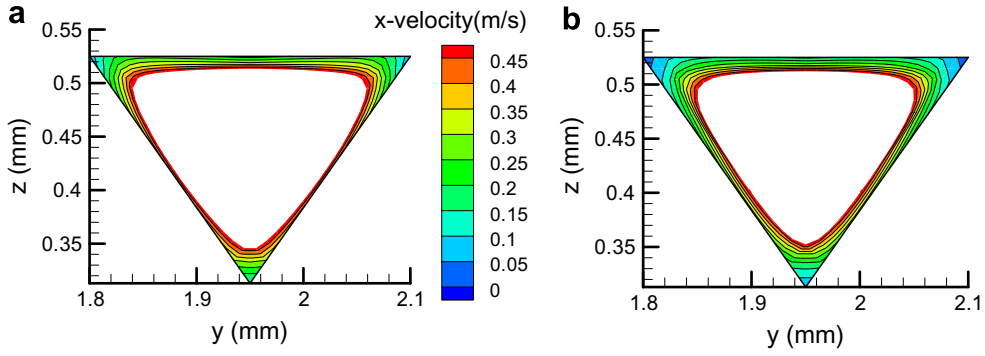

Fig. 7. Velocity near the solid wall surface. (a) Distribution at the entrance of zone 3 for run 17*, Re_m = 210 and (b) Distribution near the solid wall surface at the corresponding locations for run 17, Re_m = 210.

6. Results and discussion

6.1. Validation with the classical flow and heat transfer solutions

Initially, we perform the fully developed flow computation in an isosceles triangle channel at the base angle of 54.74° for the adiabatic flow with the constant fluid physical properties. The computations yield the Poiseuille number to be 13.302. The Poiseuille number for the isosceles triangular channel can be predicted as [14]

$$Po = 13.33 \times \left[3.878\left(\frac{\sin\theta - \tan(\theta/2)\cos\theta + 2\tan(\theta/2)\cos\theta\csc(\theta/2)}{6(1+\cos\theta)} - \frac{1}{3\sqrt{3}}\right) + 1\right] \quad (8)$$

Our computed Poiseuille number of 13.302 in an isosceles triangular channel agrees well with the predicted value of 13.308 by Eq. (8).

Heat transfer computations for the fully thermal developed flow were also performed in the isosceles triangular channel at the base angle of 54.74° under the constant heat flux conditions. The computed Nusselt number is $Nu_H = 3.110$ with three heated sides of the channel, which is very close to the value of 3.093 given in Ref. [14] for the same condition. The Nusselt number is 2.765 for the constant heat flux condition with two heated sides, and this value is taken as the reference for comparisons in the present study.

6.2. Validation with our experimental data

Totally we performed the liquid flow and heat transfer experiments for 74 runs. The runs that were involved in the present paper are listed in Table 2, with the superscript * indicating those for the interrupted microchannel heat sink. A pair of runs shares similar operating parameters for the two heat sinks, but they are not exactly identical due to the experiment difficulties. It is found from Table 2 that the computed pressure drops are slightly larger than the measured values by less than 10% for most runs.

We compare our numerical simulations with experimental measurements, which are shown in Fig. 4 for run 17*. Fig. 4a illustrates the measured chip temperatures over the thin film heating area (16.0mm by 4.2mm), which is visualized by the IR image system. But Fig. 4b shows the computed temperatures of the back surface over the whole silicon chip. A gradual increase in temperatures along the flow direction is observed for both the measured and computed values. Fig. 4c gives the two-dimensional comparisons of temperatures along the flow direction at specific width locations. The temperatures at the centerline of y/W=0.5 are slight larger than those at the quarter-line of y/W=0.25. The computed temperatures are slightly larger than the measured values by less than a couple of degrees, due to the uncertainty of natural convection heat transfer coefficient used.

6.3. Multi-channel effect of flow and heat transfer in microchannels

We identified multi-channel effect of flow rates in each channel and heat received by different channels, as shown in Fig. 5(a–b). Both mass flux and heat obey the parabola curve distribution versus channel numbers, with the center channels of 5 and 6 having about 0.2% larger mass fluxes than the average value, and the side channels of 1 and 10 having 0.3% to 0.4% lower mass fluxes than the average value, for the three runs of 17, 19 and 21. Meanwhile, heat received by the center channel is about 2% larger than the average value, it is lower by about 2% than the average value for the side channels of 1 and 10. Under the high, uniform heat flux on the thin film heater surface, heat conduction in solid silicon from the center to the side of the chip in the width direction yields slight larger heat received by the center channels. Due to the coupled heat transfer and flow rate, the slight larger heat and temperature in center channels lead to lower viscosities, yielding slight larger mass fluxes in center channels to balance pressure drops among different channels.

For the interrupted microchannel heat sink, zones 2, 3, 4 and 5 are in the heating area while zones 1 and 6 are out of the heating area (see Fig. 1b). The longitudinal microchannels in zones 2 to 5 have similar distributions of mass fluxes and received heat among different channels as those for the conventional microchannel heat sink. Slight larger mass fluxes in center channels in zone 2 correspond to slight higher pressures in the microchamber center following zone 1, reducing effective pressure differences for the center longitudinal microchannels in zone 1, causing an inverse mass flux distribution in zone 1 as that in the conventional microchannel heat sink. That is, mass fluxes are slight smaller in the center channels in zone 1. Heat received in zone 1 is due to the thermal conduction of silicon, having the similar distribution as that for the conventional microchannel heat sink. Usually, mass flux and heat obey the symmetry distributions. The slight asymmetry channel arrangement in the chip width direction may cause the mass flux and heat flux distribution deviated from the exact symmetry. As shown in Fig. 2a, the margin of region 1 is slightly larger than that of region 6 in the chip width direction.

In summary, for both heat sinks mass fluxes have very small differences among different channels and could be neglected. The re-

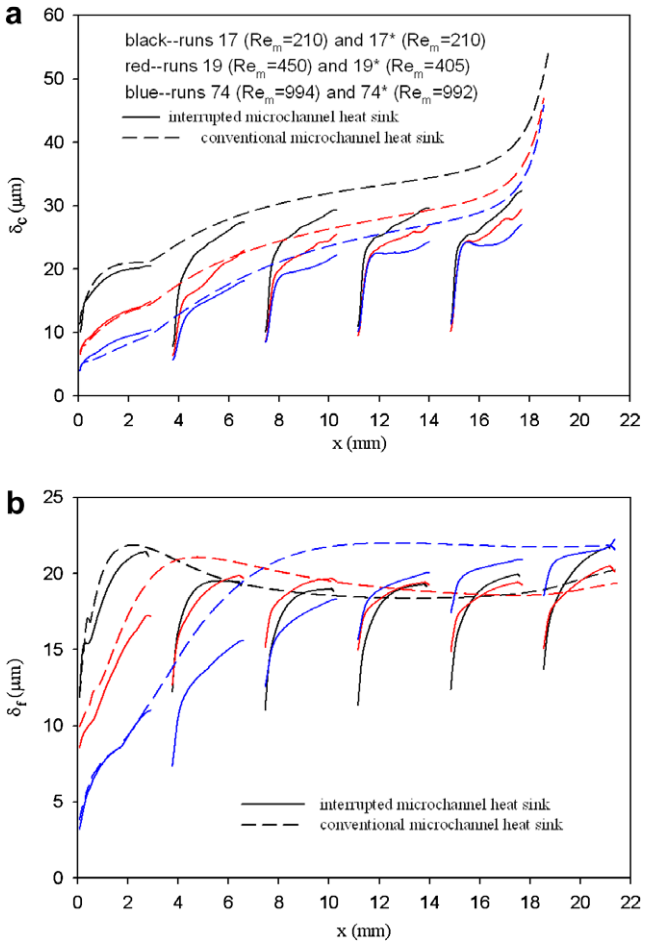

Fig. 8. The thermal and hydraulic boundary layer thickness along the flow direction for the two microchannel heat sinks.

ceived heat by different channels accounts for 2% deviation from the averaged value when the project heat flux reaches 100 W/cm^2.

6.4. Flow and heat transfer in the two microchannel heat sinks

For both heat sinks, there is no thermal boundary layer close to the glass cover because such surface is adiabatic, except in the corners of triangular channels. Fig. 6a gave the temperature distribution close to the two side walls within the temperature variations in ten degrees at the entrance of zone 3 (see Fig. 1b), for the interrupted microchannel heat sink. The thermal boundary layers are thin and the temperature gradients are large close to the two side walls, especially at the center of side walls, significantly enhancing heat transfer there. Fig. 6b shows the temperature variations close to the side walls for the conventional microchannel heat sink at the same axial location, indicating the thicker boundary layer and smaller temperature gradient. Temperature distributions for the interrupted microchannel heat sink in channels at the entrances of zone 2, 4, 5 are similar to Fig. 6a. Fig. 6 gives the strong evidence that the thermal boundary layer is redeveloping when liquid leaves a microchamber and enters the following zone, being responsible for the heat transfer enhancement for the newly proposed microchannel heat sink.

Fig. 7a shows the velocity profiles at the entrance of zone 3 for the interrupted microchannel heat sink, while Fig. 7b gives such distributions for the conventional microchannel heat sink. Velocities are only shown in the range of 0 to 0.45m/s. The velocity gradient is larger and the hydraulic boundary layer is thinner at the entrance of each separated zone for the interrupted microchannel heat sink. Velocity profiles in channels at the entrances of zone 2, 4, 5, 6 for the interrupted microchannel heat sink are similar to Fig. 7a.

The thicknesses of thermal and hydraulic boundary layers at the center of left side wall for the channel 5 are shown in Fig. 8, for three group runs of 17 and 17*, 19 and 19*, 74 and 74*, respectively. Each group run for the two heat sinks shares one color. The x coordinate starts from $x = 0$, i.e., the first zone entrance (see Fig. 1). However, the development of thermal boundary layer (Fig. 8a) is only plotted for the upstream five zones but the hydraulic one is plotted for all the six zones (Fig. 8b). This is because the zone 6 is out of the heating area, in which the temperature gradient is very small and the thermal boundary layer almost occupies the whole channel cross section there. Fig. 8a shows that the thickness of thermal boundary layer has a sharp increase when liquid just leaves zone 5 for the conventional microchannel heat sink, due to the sharply reduced temperature gradient there. Once liquid is flowing out of the heating zone 5, the heat transfer in microchannels is coupled with the silicon thermal conduction and flow rates. The development of thermal boundary layer in the first zone is due to the heat conduction, which is almost identical for both two heat sinks. However, the thermal boundary layer is redeveloping in zones 2, 3, 4 and 5 for the interrupted microchannel heat sink. The thermal boundary layer is not fully developed for the conventional microchannel heat sink, due to the larger Prandtl number of water.

Fig. 8b shows the development of hydraulic boundary layers for the three group runs. The thickness of hydraulic boundary layer attains a constant when $x > 10$ mm for run 74, having larger mass

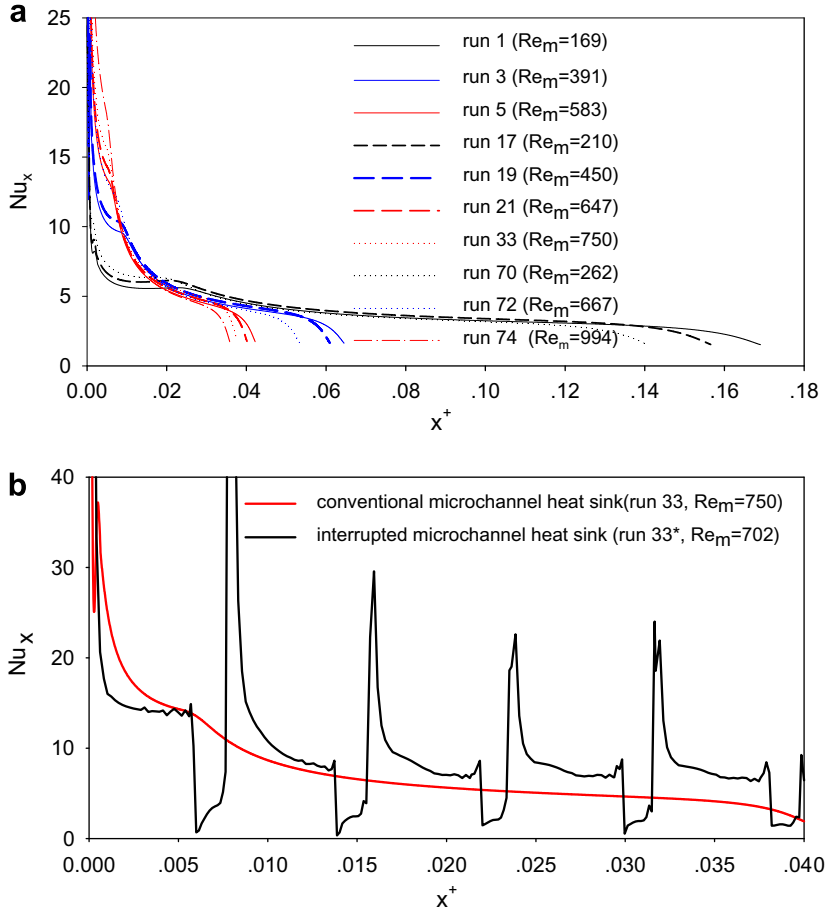

Fig. 9. Cross-sectional average, but axial flow dependent Nusselt numbers versus non-dimensional flow length for the two microchannel heat sinks.

flux and lower heat flux, leading to smaller liquid temperature difference between inlet and outlet, indicating the smaller physical property effect. However, the thicknesses of hydraulic boundary layer are increased and attain a maximum value in the microchannel upstream, followed by a slight parabola distribution for runs 17 and 19. Lower mass fluxes for the two runs lead to fast development of hydraulic boundary layer. Meanwhile, larger liquid temperature difference between inlet and outlet (see Table 2) ensures the physical property effect on the development of hydraulic boundary layer. As expected for the interrupted microchannel heat sink, the hydraulic boundary layer is redeveloping in each separated zone for runs 17^*, 19^* and 74^*. The thickness is small when liquid is just entering a new zone, increased and even larger than that for the conventional microchannel heat sink in zones 3, 4, 5 and 6 for runs 17^* and 19^*. This is because the flow length is shortened and the physical property effect is not significant in each zone for the interrupted microchannel heat sink. As expected, the maximum thickness of hydraulic boundary layer in each zone should be decreased to that of the conventional microchannel heat sink if each zone length be increased.

Even though the two heat sinks have the same geometry sizes except that the longitudinal microchannels are separated into several parts for the interrupted microchannel heat sink, the definitions of Nu_x and x^+ are identical, noting that the maximum x^+ is different from run to run. Fig. 9a shows that curves of the axial Nusselt numbers shrink into one, except at the short entrance region and the ending unheated region, for the conventional microchannel heat sink. Fig. 9b shows Nu_x versus $x^+$for the two heat sinks. Run 33 and 33^* share similar running parameters. Nu_x is significantly high and has a decrease in each separated zone, but is always larger than that for the conventional microchannel heat sink. The Nusselt number in microchambers is found to be significantly lower than that of conventional microchannel heat sink. The reduced shear stress in microchambers deteriorates heat transfer in these areas. In other words, microchambers contribute less to the heat transfer. The heat transfer enhancement is mainly caused by the repeated redeveloping thermal boundary layers. It is noted that liquid may not be fully mixed in microchambers, due to laminar flow and short microchamber length. The degree at which the liquid deviates from the fully mixed condition depends on Reynolds number and microchamber length.

Fig. 10 shows the pressure distribution at the centerline of channel 5 along the whole flow direction. The pressure variation in the chip width direction is quite small. Because the outlet of silicon chips has atmosphere pressure, the vertical coordinate of p_r is the absolute pressure subtracting the atmosphere pressure. The x coordinate starts from $x = -4.275$ mm at the entrance of silicon chips and ends at $x = 25.725$ mm for the silicon chip exit. The referenced pressure of p_r at $x = -4.275$ mm is the total pressure drop across the whole silicon chip. For the conventional microchannel heat sink, the pressure is continuously decreased by a frictional pressure loss and a head loss in the inlet fluid plenum, a frictional pressure loss along the microchannel, a head loss and a frictional pressure loss in the outlet plenum. Pressure drop across the inter-

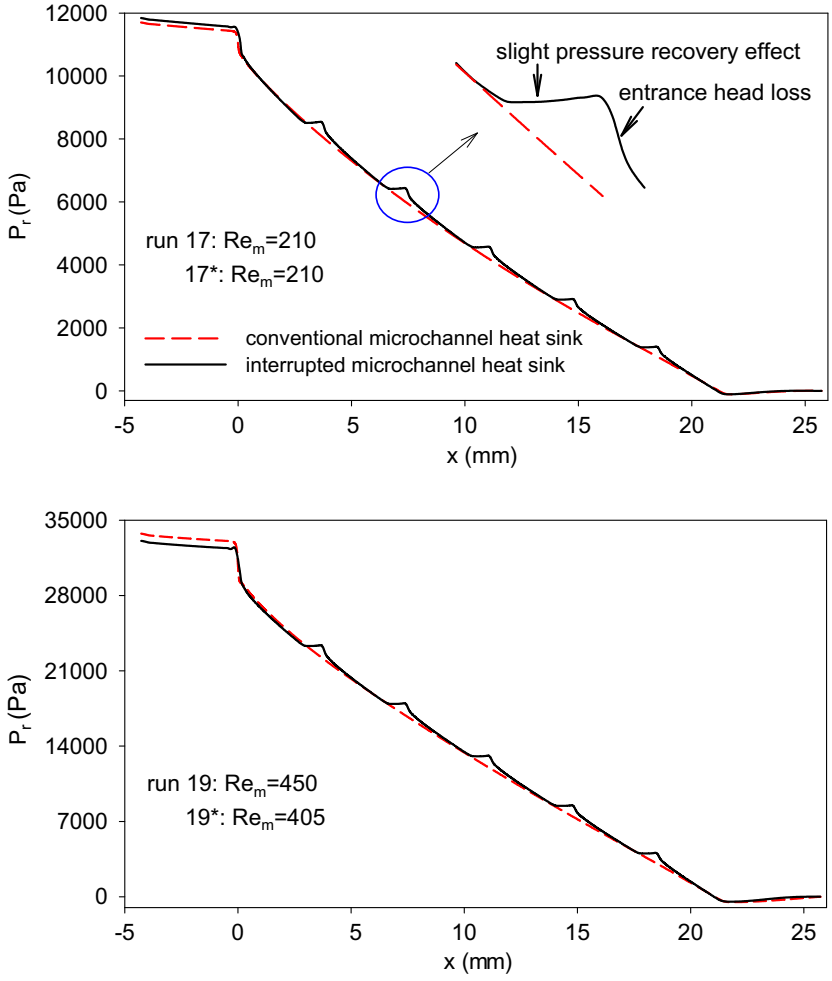

Fig. 10. Pressure distribution along the flow direction for the two microchannel heat sinks.

rupted microchannel heat sink consists of not only the terms in the inlet and outlet plenums, but also the pressure drop in microchambers. Two effects affect the pressure drop in microchambers. The first one is that the pressure has a slight increase when liquid leaves the upstream microchannels and mixes in the microchamber, identified as the pressure recovery effect in Fig. 10 caused by the Bernoulli effect. The second is the head loss when liquid leaves the microchamber and enters the following zone, identified by a steep decrease slope in Fig. 10. Depending on flow rates and microgeometry sizes, the first effect compensates or suppresses the second one, leading to almost the same pressure drop for the two heat sinks (Fig. 10a), or the decreased pressure drop for the interrupted microchannel heat sink than the conventional one (Fig. 10b).

6.5. Overall thermal and flow performance for the two heat sinks

Here we give the overall thermal and flow performance for the two heat sinks, to identify benefits that the newly proposed heat sink provides. Fig. 11 shows the averaged Nusselt number versus

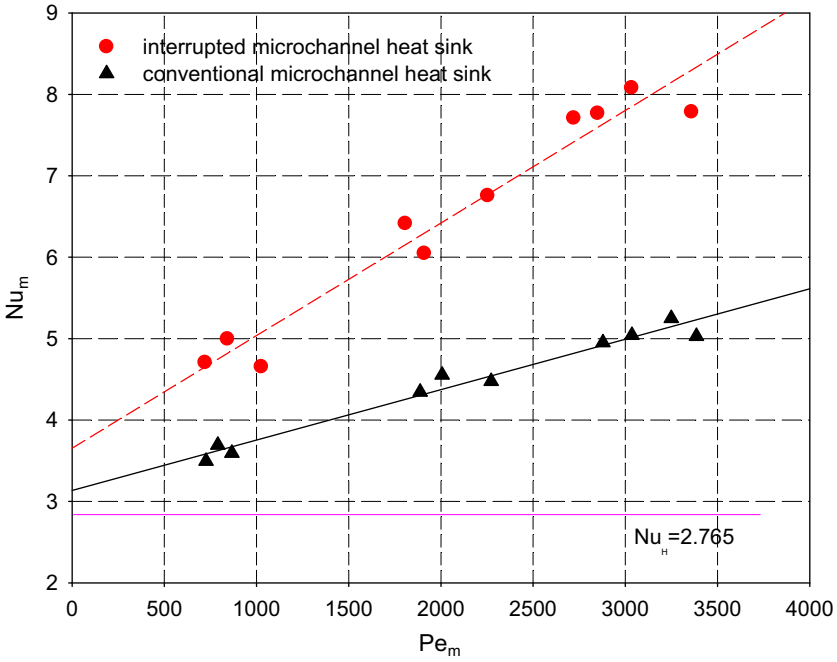

Fig. 11. Average Nusselt number versus the Peclet number for the two microchannel heat sinks.

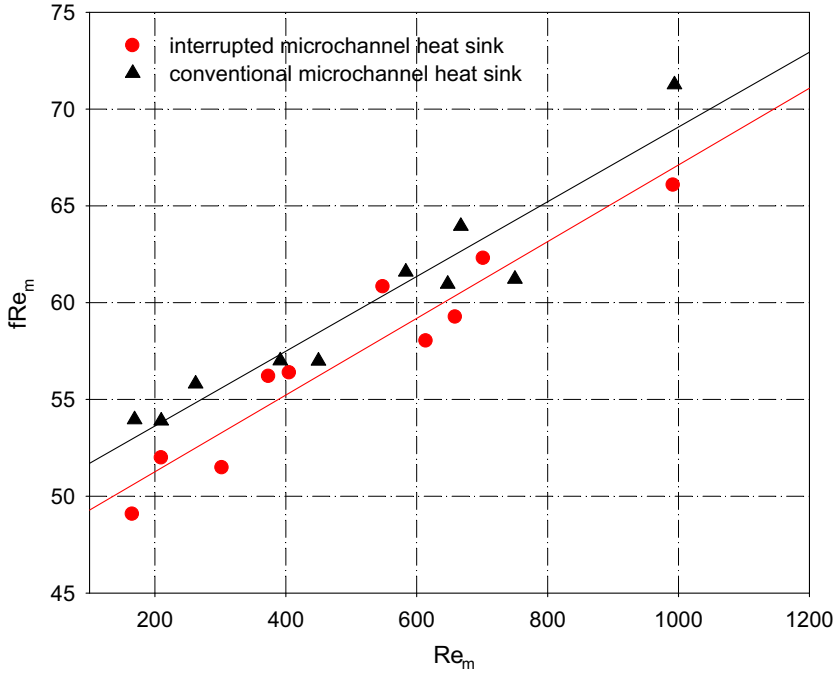

Fig. 12. The overall flow resistances versus Reynolds number for the two microchannel heat sinks.

the Peclet number, which is defined in terms of the averaged liquid temperature of inlet and outlet, covering the range of 721–3386. The Reynolds number is in the range of 169–994, ensuring laminar flow in microchannels. Heat transfer is enhanced remarkably for the interrupted microchannel heat sink than the conventional one. For instance, the average Nusselt number reaches about 8 for the interrupted microchannel heat sink, significantly larger than 5 for the conventional one, at $Pe_m = 3000$. The heat transfer enhancement strongly depends on the Peclet number. Larger Peclet number leads to greater Nusselt number differences between the two heat sinks. All the Nusselt numbers for both heat sinks are larger than that of 2.765 for the constant heat flux boundary condition with two heated sides in triangular channels at the base angle of 54.74°, inferring that the thermal boundary layer is not fully developed even for the conventional microchannel heat sink.

We give the flow resistance of fRe_m versus Reynolds number in Fig. 12. It is found that fRe_m is increased with Reynolds numbers according to the linear curve for the two heat sinks, with lower values for the interrupted microchannel heat sink than those for the conventional one.

In summary, we proposed a new microchannel heat sink, dividing the whole longitudinal microchannels into several parts by a set a transverse microchambers. Such a microdevice cannot only enhance heat transfer but also decrease pressure drop, or at least does not increase the pressure drop. This changes the strict criterion that we should decrease the channel size to enhance heat transfer, but should accompany an increase in the pressure drop and pumping power.

The newly proposed microchannel heat sink is suitable for the fluid Prandtl number larger than unity. This is because the hydraulic and thermal entrance lengths are proportional to D_hRe and D_hRePr, respectively. The two boundary layers are developing at the same speed with the fluid Prandtl number of unity. At the Prandtl number smaller than unity, the hydraulic boundary layer is developing more slowly than the thermal boundary layer. Under such circumstances, separating the entire longitudinal microchannels into a set of isolated parts enhances heat transfer. However, the slow development of hydraulic boundary layer in each separated zone results in higher pressure drop, finally leading to an increase in the total pressure drop across the silicon chip. The heat transfer and flow performances are also related to the dimensions of interrupted microchannel heat sink, which are expected to be studied in the future.

7. Conclusions

The new conclusions drawn in this paper are summarized as follows:

(1) Flow rate variations in different channels are very small and can be neglected, while the received heat by different channels accounts for 2% deviations when the project heat flux reaches 100 W/cm^2 for both heat sinks.

(2) The hydraulic and thermal boundary layers are redeveloping in each separated zone for the interrupted microchannel heat sink, with the slower development of thermal boundary layer than that of hydraulic boundary layer. The repeated thermal developing flow enhances the overall heat transfer in such a heat sink.

(3) There are two effects influencing pressure drops across the newly proposed silicon chips. The first one is the pressure recovery effect when liquids leaves the upstream zone and mixes in the microchamber, while the second one is the increased head loss once liquid enters the next zone. The first effect compensates or suppresses the second one, leading to the similar or reduced pressure drop for the interrupted microchannel heat sink than that for the conventional one.

Acknowledgements

The work is supported by the National Natural Science Foundation of China (50476088), and the Shanghai key discipline project (T0503).

References

[1] M. Kay, M.E. Crawford, Convective Heat and Mass Transfer, McGraw Hill, New York, 1980.
[2] Y. Mishan, A. Mosyak, E. Pogrebnyak, G. Hetsroni, Effect of developing flow and thermal regime on momentum and heat transfer in micro-scale heat sink, Int. J. Heat Mass Transfer 50 (2007) 3100–3114.
[3] H. Al-Bakhit, A. Fakheri, Numerical simulation of heat transfer in simultaneously developing flows in parallel rectangular ducts, Appl. Therm. Eng. 26 (5–6) (2006) 596–603.
[4] G. Gamrat, M. Favre-Marinet, D. Asendrych, Conduction and entrance effects on laminar liquid flow and heat transfer in rectangular microchannels, Int. J. Heat Mass Transfer 48 (2005) 2943–2954.
[5] G.L. Morini, M. Spiga, The role of the viscous dissipation in heated microchannels, J. Heat Transfer, ASME 129 (2007) 308–318.
[6] G.L. Morini, L. Baldas, Laminar forced convection of liquid flows through silicon microchannels, Houille Blanche-Revue Internationale de l'Eau 1 (2006) 20–25.
[7] G.L. Morini, Viscous heating in liquid flows in microchannels, Int. J. Heat Mass Transfer 48 (2005) 3637–3647.
[8] J. Koo, C. Kleinstreuer, Viscous dissipation effects in microtubes and microchannels, Int. J. Heat Mass Transfer 47 (2004) 3159–3169.
[9] J.T. Liu, X.F. Peng, W.M. Yan, Numerical study of fluid flow and heat transfer in microchannel cooling passages, Int. J. Heat Mass Transfer 50 (2007) 1855–1864.
[10] J. Li, G.P. Peterson, P. Cheng, Three-dimensional analysis of heat transfer in a micro heat sink with single phase flow, Int. J. Heat Mass Transfer 47 (2004) 4215–4231.
[11] S.V. Garimella, V. Singhal, Single phase flow and heat transport and pumping consideration in microchannel heat sinks, Heat Transfer Eng. 25 (2004) 15–25.
[12] J.L. Xu, Y.H. Gan, D.C. Zhang, X.H. Li, Microscale heat transfer enhancement using thermal boundary redeveloping concept, Int. J. Heat Mass Transfer 48 (2005) 1662–1674.
[13] F. Incropera, Liquid Cooling of Electronic Devices by Single-Phase Convection, Wiley, 1999.
[14] A. Tirunarayanan, A. Ramachandran, Frictional pressure drop in laminar and turbulent flow in isosceles triangular ducts, American Society Mechanical Engineering Report, 67-FE-18, 1967.